



UNIVERSITY OF LEEDS

This is a repository copy of *Discrete Hall resistivity contribution from Néel skyrmions in multilayer nanodiscs*.

White Rose Research Online URL for this paper:

<https://eprints.whiterose.ac.uk/130027/>

Version: Accepted Version

---

**Article:**

Zeissler, K [orcid.org/0000-0002-2698-3493](https://orcid.org/0000-0002-2698-3493), Finizio, S [orcid.org/0000-0002-1792-0626](https://orcid.org/0000-0002-1792-0626), Shahbazi, K [orcid.org/0000-0002-1082-4535](https://orcid.org/0000-0002-1082-4535) et al. (10 more authors) (2018) Discrete Hall resistivity contribution from Néel skyrmions in multilayer nanodiscs. *Nature Nanotechnology*, 13. pp. 1161-1166. ISSN 1748-3387

<https://doi.org/10.1038/s41565-018-0268-y>

---

© 2018, Springer Nature. This is an author produced version of a paper published in *Nature Nanotechnology*. Uploaded in accordance with the publisher's self-archiving policy.

**Reuse**

Items deposited in White Rose Research Online are protected by copyright, with all rights reserved unless indicated otherwise. They may be downloaded and/or printed for private study, or other acts as permitted by national copyright laws. The publisher or other rights holders may allow further reproduction and re-use of the full text version. This is indicated by the licence information on the White Rose Research Online record for the item.

**Takedown**

If you consider content in White Rose Research Online to be in breach of UK law, please notify us by emailing [eprints@whiterose.ac.uk](mailto:eprints@whiterose.ac.uk) including the URL of the record and the reason for the withdrawal request.



[eprints@whiterose.ac.uk](mailto:eprints@whiterose.ac.uk)  
<https://eprints.whiterose.ac.uk/>

## Discrete Hall resistivity contribution from Néel skyrmions in multilayer nanodiscs

Katharina Zeissler<sup>1\*</sup>, Simone Finizio<sup>2</sup>, Kowsar Shahbazi<sup>1</sup>, Jamie Massey<sup>1</sup>, Fatma Al Ma'Mari<sup>1,3</sup>, David Bracher<sup>2</sup>, Armin Kleibert<sup>2</sup>, Mark C. Rosamond<sup>4</sup>, Edmund H. Linfield<sup>4</sup>, Thomas A. Moore<sup>1</sup>, Jörg Raabe<sup>2</sup>, Gavin Burnell<sup>1</sup>, and Christopher H. Marrows<sup>1</sup>

<sup>1</sup>*School of Physics and Astronomy, University of Leeds, Leeds LS2 9JT, United Kingdom*

<sup>2</sup>*Swiss Light Source, Paul Scherrer Institut, Villigen 5232, Switzerland*

<sup>3</sup>*Department of Physics, Sultan Qaboos University, 123 Muscat, Oman*

<sup>4</sup>*School of Electronic and Electrical Engineering, University of Leeds, Leeds LS2 9JT, United Kingdom*

\*Correspondence to [k.zeissler@leeds.ac.uk](mailto:k.zeissler@leeds.ac.uk)

Magnetic skyrmions are knot-like quasiparticles. They are candidates for non-volatile data storage in which information is moved between fixed read and write terminals. Read-out operation of skyrmion-based spintronic devices will rely upon electrical detection of a single magnetic skyrmion within a nanostructure. Here, we present Pt/Co/Ir nanodiscs which support skyrmions at room temperature. We measured the Hall resistivity whilst simultaneously imaging the spin texture using magnetic scanning transmission x-ray microscopy (STXM). The Hall resistivity is correlated to both the presence and size of the skyrmion. The size-dependent part matches the expected anomalous Hall signal when averaging the magnetisation over the entire disc. We observed a resistivity contribution which only depends on the number and sign of skyrmion-like objects present in the disc. Each skyrmion gives rise to  $22 \pm 2$  n $\Omega$  cm irrespective of its size. This contribution needs to be considered in all-electrical detection schemes applied to skyrmion-based devices.

The non-trivial topology of a skyrmion leads to an improved stability against external perturbations<sup>1, 2, 3, 4, 5</sup>. The topology of the spin texture is characterised by the skyrmion winding number  $S$ , which takes integer values<sup>6</sup>. Mathematically,  $S$  is given by<sup>1</sup>,

$$S = \frac{1}{4\pi} \int \mathbf{m} \cdot \left( \frac{\partial \mathbf{m}}{\partial x} \times \frac{\partial \mathbf{m}}{\partial y} \right) dx dy, \quad (1)$$

where  $\mathbf{m}$  is a unit vector pointing along the local magnetisation direction. Individual cylindrical skyrmions have a winding number of  $\pm 1$ .  $S$  is an integer invariant for all mutually continuously deformable skyrmions. Hence, the associated topological Hall effect is also invariant under continuous deformation. A consequence of this, in the context of Néel skyrmions, is that the winding number is magnetic domain size and shape independent as long as the domain is wrapped by an unbroken Néel domain wall<sup>1</sup>. In multilayer films the formation of Néel type skyrmions is energetically favourable due to perpendicular magnetic anisotropy, interface Dzyaloshinskii-Moriya and dipolar interaction<sup>7, 8, 9, 10, 11</sup>. In thin film multilayers they are stable at room temperature<sup>11, 12, 13</sup> and can be moved using spin-torques<sup>14, 15, 16, 17, 18</sup>, with the expectation that the current densities needed can eventually be as low as the  $10^6$ - $10^7$  A/m<sup>2</sup> observed in cryogenic measurements on single crystal materials<sup>19, 20, 21</sup>. This permits very low energy manipulation of information<sup>22</sup>. Whilst current-induced movement of skyrmions is needed to manipulate the encoded information, electrical detection of single skyrmions is essential to read back the stored information.

Here we have measured the Hall resistance of Pt/Co/Ir multilayer discs of 1  $\mu\text{m}$  diameter while simultaneously imaging the magnetic configuration within it using STXM with x-ray magnetic circular dichroism (XMCD) contrast. STXM is a high resolution imaging technique which is magnetically non-invasive. The conclusions that we draw are twofold. The variation in skyrmion size with field leads to

a signal that matches that expected from the anomalous Hall effect tracking the change in magnetisation. Furthermore, an additional magnetisation-independent Hall signal of  $22 \pm 2$  n $\Omega$  cm associated with the presence, number, and sign of individual skyrmion-like objects was found. Its size is comparable to the anomalous Hall signal for skyrmions with a radius smaller than  $150 \pm 30$  nm. This skyrmion number-dependent resistivity cannot qualitatively be explained with conventional Berry phase theories of the topological Hall effect, suggesting that further theoretical development is needed.

Skyrmions and skyrmion-like domains were stabilised in an electrically connected 1  $\mu$ m diameter discs from [Pt/Co/Ir]<sub>x10</sub> multilayer stacks (see supplementary information, figure S1, for device, magnetic and electrical information). A current and field nucleation protocol was used to nucleate an integer number of skyrmions in the disc (see methods section and supplementary information, figure S2 for details). The Hall resistance was measured as a function of out-of-plane field. From the XMCD contrast images the normalised magnetisation was computed by counting the number of black, white, and grey pixels in the disc and assigning them a value of 1, -1, and 0 respectively and normalising the sum by the number of pixels in the disc (see supplementary information for details, figure S3). Figure 1 (a) - (c) shows the electrical and magnetic response to an external out of plane field of one skyrmion,  $N = 1$ , stabilised in the discs. The number  $N$  is a counter of enclosed magnetic domains without drawing conclusions on their topology. In case of a skyrmion,  $N = -S$  is the sign convention adopted throughout this paper. The distinction between  $S$  and  $N$  becomes relevant when considering magnetic domains which touch the edge in such a way that the Néel domain wall wrapping is incomplete or when the wrapping is disrupted locally by, for example, a Bloch point. Measuring the Hall resistance throughout magnetic minor loops enabled the observation of changes in the resistance reflected by changes in the magnetic state while keeping the number of skyrmions in the disc constant was kept constant. The Hall resistance, the corresponding skyrmion diameter and normalised disc magnetisation throughout two minor loops are shown in figure 1 (a)-(c) alongside XMCD images of the domain states (d)-(g) and (h)-(i). In the final field sweep of Repeat 1 the applied field was increased until the skyrmion was annihilated (Major loop 6, figure 1(a)-(c)), which took place between 65 and 70 mT and reduced the value of  $N$  from 1 to 0. After the skyrmion is annihilated the Hall resistivity returns to its saturation value of around  $-223 \pm 6$  n $\Omega$  cm. A clear resistivity change with respect to the saturation value was observed for skyrmions with a diameter above 75 nm. XMCD images of skyrmion states corresponding to  $N = -2, 2$  and  $3$  are seen in figure 2 (a)-(c), (e)-(g) and (i)-(k) respectively with the normalised magnetisation  $M_z/M_{Sat}$  and the change in the normalised Hall resistance  $R_{xy}/R_{xy,Sat}$  response (d), (h) and (l) respectively. See supplementary information movies for all XMCD images measured.

In magnetic materials with topologically non-trivial spin textures, the Hall resistivity is given by the sum of the ordinary ( $\rho_{xy}^N$ ), the anomalous ( $\rho_{xy}^A$ ), and the topological ( $\rho_{xy}^T$ ) Hall resistivities<sup>6</sup>,

$$\rho_{xy} = \rho_{xy}^N + \rho_{xy}^A + \rho_{xy}^T = R_0 B + R_S \mu_0 M_z + R_0 P B_{eff}^z, \quad (2)$$

where  $R_0$  is the ordinary Hall coefficient,  $B$  is the external applied magnetic field,  $R_S$  is the anomalous Hall coefficient,  $M_z$  is the z-component of the magnetisation,  $P$  is the spin polarisation of the conduction electrons, and  $B_{eff}^z$  is the effective field experienced by the conduction electrons due to Berry phase they accumulate whilst adiabatically traversing skyrmions<sup>23, 24</sup>. This magnetic field emerges as there is one quantum of emergent magnetic flux associated with each skyrmion<sup>6, 25</sup>. In this form, Equation (1) neglects any other contributions such as the planar Hall effect, which can arise due to anisotropic magnetoresistance mechanism.

Figure 3 (a) shows the normalised Hall resistance  $R_H/R_{H,Sat}$  against the normalised magnetisation  $M_z/M_{Sat}$ . The ordinary Hall resistance contribution was calculated using the measured ordinary Hall coefficient of  $-1.9 \pm 0.2 \times 10^{-11}$   $\Omega$ m/T and was subtracted from the measured value  $R_{xy}$  to yield  $R_H$ .

Therefore, in accordance with equation 1, changes in  $R_H$  arise only from changes in the magnetisation and/or spin texture.

Eq. 1 shows that the anomalous Hall resistivity  $\rho_{xy}^A$  is expected to be proportional to the  $z$ -component of the magnetisation, the same component that gives rise to XMCD contrast in the STXM setup. This condition is true if there are no changes in the longitudinal resistivity, since  $R_s$  typically has a dependence on  $\rho_{xx}$ . As different magnetic states are measured in the same discs and at the same temperature, and the magnetoresistance is vanishingly small, this condition holds. The line connecting the two saturated states was fitted, shown in figure 3(a) yielding a slope of  $-1.01 \pm 0.01$  and an intercept of  $0.01 \pm 0.05$ . This slope is within the error bar of  $-1$ ; the value expected on the basis of the Hall signal being purely due to an anomalous Hall effect arising from the magnetisation averaged over the area of the disc. All other data for  $N > 0$  and  $N < 0$  run parallel to this line i.e. retaining a slope of  $-1$  (see figure 3(b) for the fitted slopes and intercepts). All data sets are within one error bar of a  $-1$  slope except the  $N = -2$  data set which is  $-1$  within two error bars. This distribution is consistent with Gaussian statistics. We can therefore identify this variation in the Hall signal as the anomalous Hall effect associated with the skyrmion being compressed and expanded by the field. However, each data set is offset from the  $N = 0$  line i.e. each  $N \neq 0$  data set has a non-zero intercept indicating that there must be an additional  $\rho_{xy}$  resistivity contribution which is magnetisation independent.

The intercepts were converted into resistivities,  $\rho_{xy}^{\text{int}}$ , and are plotted versus  $N$  in figure 3 (b).  $\rho_{xy}^{\text{int}}$  is proportional to the number of skyrmion-like objects  $N$  in the disc. The dashed line shows the linear fit through the data points and reveals that each skyrmionic object contributes  $22 \pm 2$  n $\Omega$ cm to the measured resistivity.

Figure 3 (c) shows  $\rho_{xy}^{\text{int}}$ , with respect to sequential image numbers. This highlights the skyrmion number dependent incremental change away from the  $N = 0$  case. The XMCD images shown in figure 3 (d) to (o) highlight the magnetisation independence of the measured offset. The offset is the same for the same number of skyrmions  $N$  even when they have very different sizes, compare the states depicted in figure 3(d) and (e), for instance. A sharp drop in the measured offset is observed when one of the following two magnetic field driven scenarios occur (i) the individual skyrmions expand and fuse together (see figure 3 (c) data points enclosed in the blue box and its corresponding magnetic state figure 3 (f)) and (ii) the skyrmions are annihilated (see figure 3 (c) data points enclosed in the green and red box, the corresponding magnetic state of the latter can be seen in figure 3 (i)).

Images within the  $N = 3$  data set indicate that there is a possibility that the magnetic domains are touching the edge for certain fields (see figure 2 (i)-(k)). The imaging resolution and the parasitic x-ray absorption at the electrodes makes it hard to identify whether the domain is continuously wrapped by a Néel domain wall or whether the domain wall has been ejected at the edge, i.e. whether  $S = N$  or whether  $S \neq N$ . Whilst the STXM shows only the out-of-plane component of the magnetisation, imaging of the in-plane magnetisation and hence the confirmation of Néel type domain walls in these multilayer systems was done using photoemission electron microscopy on films grown at the same time as the disc samples. Left-handed Néel domain walls were observed (see supplementary information figure S4). This is in agreement with Lorentz microscopy under tilted imaging conditions on closely related material grown in the same sputter system<sup>26</sup>, as well as previous results from Chauleau et al. on multilayers with the same stacking sequence<sup>27</sup>. Such domain walls form topologically non-trivial skyrmionic spin textures when appearing as closed loops. No change in  $\rho_{xy}^{\text{int}}$  was observed until the magnetic domains were seen to annihilate or coalesce (see figure 3 (c) green, red and blue boxes and (f)) from which we conclude that either the domains remain completely wrapped by Néel domain walls and that  $S = N$ , or that the physical origin of the magnetisation independent contribution is not reliant on an integer value for  $S$ .

Returning again to Eq. 2, it is tempting to identify this signal that occurs when the topology changes as the topological Hall effect  $\rho_{xy}^T$ , since the emergent field is proportional to the areal winding number density in that theory. The usual theory of that effect states that the change in the resistivity associated with the presence of skyrmions can be estimated using

$$\rho_{xy}^T \approx PR_0 \left| \frac{q^e}{e} \right| B_z^e = PR_0 \phi_0 S/A, \quad (3)$$

where  $q^e$  is the emergent topological charge equal to  $\pm \frac{1}{2}$  for different spins, and  $B_z^e$  is the emergent magnetic field given by  $(\hbar/2)8\pi\phi_z$  ( $\phi_z$  is the skyrmion density  $S/A$ ),  $A$  is the area of the disc, and  $\phi_0$  is the flux quantum  $h/e$  with  $h$  being Planck's constant and  $e$  the electron charge<sup>20, 23, 28</sup>. In our case, using a maximum possible spin polarization of 100 %,  $\rho_{xy}^T$  can be computed from this expression to have an upper limit of 0.01 n $\Omega$  cm per skyrmion in the disc. This value, despite representing the maximum expected by current theory, is far too small to account for the observed signal. On the other hand, other effects might be involved. Distortions in the current flow around the skyrmion due to the current-focussing effects arising from the anisotropic magnetoresistance (AMR)<sup>29</sup>, the planar Hall effect<sup>30</sup>, or d.c. eddy current loops<sup>31</sup> may also play a role in generating transverse voltages. Contributions from the planar Hall effect can be ruled out as it is a consequence of AMR. Local changes of the in plane magnetisation with respect to the current direction result in a change of the resistivity which then leads to a redistribution of the current density and hence the voltage equipotential measured. The AMR is even in magnetisation and hence  $N = 2$  and  $N = -2$  states (such as those shown in figure 3(h) and (n)) would show the same sign of planar Hall effect contribution, whilst an opposite sign is observed. Furthermore, the measured AMR ratio for the multilayer system is 0.04 %, whilst an effect at the level of 15% is required to generate a planar Hall resistivity at the level of the observed  $\rho_{xy}^{\text{int}}$  (see supplementary information for details, figure S5). D.c. eddy current loops are again a consequence of AMR and hence cannot produce the required magnitude. Eddy current loops are present in 180° walls, however a skyrmion can be viewed as a 360° wall i.e. two 180° walls, one up-down and one down-up, back-to-back, and hence any d.c. eddy current loops will cancel. Furthermore, any distortions in the current distribution caused by the AMR will be skyrmion-size dependent, whilst we see a constant  $\rho_{xy}^{\text{int}}$  for rather different skyrmion sizes with the same  $N$  (see for instance states in figure 3(d) and (e)). Another explanation is therefore needed, and our results challenge conventional models of the Hall effects generated by skyrmions.

The Berry phase theories above treat systems that are chemically homogeneous and have an almost uniform skyrmion winding number density arising from a skyrmion lattice. Neither of these conditions are true in our multilayer system containing discrete skyrmions in a uniform background. Moreover the transport is unlikely to be adiabatic<sup>32, 33</sup>, and the skyrmion will not be considerably smaller than the spin diffusion length in the metals from which our multilayer is formed<sup>34, 35</sup>, as is commonly assumed in such theories. Hence, a new treatment of these real space Berry phase effects in such multilayer systems is needed to clarify these points.

## CONCLUSION

Electrical transport measurements have frequently been employed to study skyrmions in bulk-DMI non-centrosymmetric transition metal compounds while the material was in the skyrmion crystal phase<sup>6</sup>. Measurements were performed on bulk samples<sup>36</sup>, single crystals<sup>20, 23, 25</sup>, thin films<sup>37, 38</sup>, and nanostructures<sup>39, 40, 41</sup>. Spin polarised scanning transmission microscopy and differential tunnelling non-collinear magnetoresistance at low temperature has been shown to allow the detection of single skyrmions in ultra-high vacuum conditions<sup>42, 43</sup>. Readout with conventional magnetic tunnel junctions has been analysed theoretically but not practically demonstrated<sup>44</sup>. As for room temperature detection, an anomalous Hall detection scheme was showcased at room temperature which confirmed that the anomalous Hall resistance can detect a single skyrmion<sup>45</sup>. By counting the skyrmion number and comparing it to the Hall resistivity conflicting conclusions have

been drawn. On one side, only the ordinary and anomalous Hall contribution could be observed<sup>45</sup>, while on the other side of the argument an additional, possibly topological, contribution was observed<sup>46</sup>.

We have performed a combined imaging and electrical transport study that allows the direct correlation of the Hall signal in a skyrmion-bearing nanostructure with the exact spin texture that gives rise to it. We have used this method to separately determine the Hall signals associated with the presence and size of skyrmions. Whilst the latter dependence arises from the anomalous Hall Effect, the former requires a new explanation. It may have the same origins as that recently reported by Raju et al.<sup>46</sup> Nevertheless, the magnetisation independence and the observed proportionality to the number of skyrmions in the disc are a good indication that the origin is linked to the non-trivial topology of the observed magnetic structures.

The size independent contribution is of great technological importance as the expected anomalous Hall resistivity associated with a skyrmion drops below the  $\rho^{\text{Int}}_{xy} = 22 \pm 2 \text{ n}\Omega \text{ cm}$  contribution when the radius is reduced below  $150 \pm 30 \text{ nm}$  (see figure 3(b)). Understanding the origin of this contribution should lead to schemes by which it may be increased to still larger amplitudes. The ability to electrically detect single skyrmions not only opens up ways to study their static and dynamic properties in nanostructures under a wide range of experimental conditions, but also offers the prospect of a simple electrical method of reading out the state of future skyrmion-based spintronic devices.

## REFERENCES

1. Braun HB. Topological effects in nanomagnetism: from superparamagnetism to chiral quantum solitons. *Adv Phys* 2012, **61**(1): 1-116.
2. Kim JV, Yoo MW. Current-driven skyrmion dynamics in disordered films. *Appl Phys Lett* 2017, **110**(13): 132404.
3. Lin SZ, Reichhardt C, Batista CD, Saxena A. Particle model for skyrmions in metallic chiral magnets: Dynamics, pinning, and creep. *Phys Rev B* 2013, **87**(21): 214419.
4. Muller J, Rosch A. Capturing of a magnetic skyrmion with a hole. *Phys Rev B* 2015, **91**(5): 054410.
5. Rohart S, Miltat J, Thiaville A. Path to collapse for an isolated Neel skyrmion. *Phys Rev B* 2016, **93**(21): 214412.
6. Nagaosa N, Tokura Y. Topological properties and dynamics of magnetic skyrmions. *Nat Nanotechnol* 2013, **8**(12): 899-911.
7. Dzyaloshinsky I. A Thermodynamic Theory of Weak Ferromagnetism of Antiferromagnetics. *J Phys Chem Solids* 1958, **4**(4): 241-255.

8. Moriya T. Anisotropic Superexchange Interaction and Weak Ferromagnetism. *Phys Rev* 1960, **120**(1): 91-98.
9. Hrabec A, Porter NA, Wells A, Benitez MJ, Burnell G, McVitie S, *et al.* Measuring and tailoring the Dzyaloshinskii-Moriya interaction in perpendicularly magnetized thin films. *Phys Rev B* 2014, **90**(2): 020402.
10. Han DS, Kim NH, Kim JS, Yin YX, Koo JW, Cho J, *et al.* Asymmetric Hysteresis for Probing Dzyaloshinskii-Moriya Interaction. *Nano Lett* 2016, **16**(7): 4438-4446.
11. Zeissler K, Mruczkiewicz M, Finizio S, Raabe J, Shepley PM, Sadovnikov AV, *et al.* Pinning and hysteresis in the field dependent diameter evolution of skyrmions in Pt/Co/Ir superlattice stacks. *Scientific Reports* 2017, **7**: 15125.
12. Legrand W, Maccariello D, Reyren N, Garcia K, Moutafis C, Moreau-Luchaire C, *et al.* Room-Temperature Current-Induced Generation and Motion of sub-100 nm Skyrmions. *Nano Lett* 2017, **17**(4): 2703-2712.
13. Moreau-Luchaire C, Moutafis C, Reyren N, Sampaio J, Vaz CAF, Van Horne N, *et al.* Additive interfacial chiral interaction in multilayers for stabilization of small individual skyrmions at room temperature (vol 11, pg 444, 2016). *Nat Nanotechnol* 2016, **11**(8): 731-731.
14. Hrabec A, Sampaio J, Belmeguenai M, Gross I, Weil R, Cherif SM, *et al.* Current-induced skyrmion generation and dynamics in symmetric bilayers. *Nat Commun* 2017, **8**: 15765
15. Jiang WJ, Zhang XC, Yu GQ, Zhang W, Wang X, Jungfleisch MB, *et al.* Direct observation of the skyrmion Hall effect. *Nat Phys* 2017, **13**(2): 162-169.
16. Litzius K, Lemesh I, Kruger B, Bassirian P, Caretta L, Richter K, *et al.* Skyrmion Hall effect revealed by direct time-resolved X-ray microscopy. *Nat Phys* 2017, **13**(2): 170-175.
17. Woo S, Litzius K, Kruger B, Im MY, Caretta L, Richter K, *et al.* Observation of room-temperature magnetic skyrmions and their current-driven dynamics in ultrathin metallic ferromagnets. *Nat Mater* 2016, **15**(5): 501-+.
18. Woo S, Song KM, Han HS, Jung MS, Im MY, Lee KS, *et al.* Spin-orbit torque-driven skyrmion dynamics revealed by time-resolved X-ray microscopy. *Nat Commun* 2017, **8**: 15573.
19. Jonietz F, Muhlbauer S, Pfleiderer C, Neubauer A, Munzer W, Bauer A, *et al.* Spin Transfer Torques in MnSi at Ultralow Current Densities. *Science* 2010, **330**(6011): 1648-1651.
20. Schulz T, Ritz R, Bauer A, Halder M, Wagner M, Franz C, *et al.* Emergent electrodynamic of skyrmions in a chiral magnet. *Nat Phys* 2012, **8**(4): 301-304.

21. Yu XZ, Kanazawa N, Zhang WZ, Nagai T, Hara T, Kimoto K, *et al.* Skyrmion flow near room temperature in an ultralow current density. *Nat Commun* 2012, **3**: 988.
22. Fert A, Cros V, Sampaio J. Skyrmions on the track. *Nat Nanotechnol* 2013, **8**(3): 152-156.
23. Neubauer A, Pfleiderer C, Binz B, Rosch A, Ritz R, Niklowitz PG, *et al.* Topological Hall Effect in the A Phase of MnSi. *Phys Rev Lett* 2009, **102**(18): 186602.
24. Tanabe K, Yamada K. Electrical detection of magnetic states in crossed nanowires using the topological Hall effect. *Appl Phys Lett* 2017, **110**(13): 132405.
25. Ritz R, Halder M, Franz C, Bauer A, Wagner M, Bamler R, *et al.* Giant generic topological Hall resistivity of MnSi under pressure. *Phys Rev B* 2013, **87**(13): 134424.
26. McVitie S, Hughes S, Fallon K, McFadzean S, McGrouther D, Krajnak M, *et al.* A transmission electron microscope study of Néel skyrmion magnetic textures in multilayer thin film systems with large interfacial chiral interaction. *Scientific Reports* 2018, **8**: 5703.
27. Chauleau JY, Legrand W, Reyren N, Maccariello D, Collin S, Popescu H, *et al.* Chirality in Magnetic Multilayers Probed by the Symmetry and the Amplitude of Dichroism in X-Ray Resonant Magnetic Scattering. *Phys Rev Lett* 2018, **120**(3): 037202.
28. Jalil MBA, Tan SG. Robustness of topological Hall effect of nontrivial spin textures. *Scientific Reports* 2014, **4**: 5123.
29. Berger L. Galvanomagnetic voltages in the vicinity of a domain wall in ferromagnetic thin films. *J Appl Phys* 1991, **69**: 1550.
30. West FG. Rotating-Field Technique for Galvanomagnetic Measurements. *J Appl Phys* 1963, **34**: 1171.
31. Berger L. Low-field magnetoresistance and domain drag in ferromagnets. *J Appl Phys* 1978, **49**: 2156.
32. Boule O, Kimling J, Warnicke P, Kläui M, Rüdiger U, Malinowski G, *et al.* Nonadiabatic Spin Transfer Torque in High Anisotropy Magnetic Nanowires with Narrow Domain Walls. *Phys Rev Lett* 2008, **101**: 216601.
33. San Emeterio Alvarez L, Wang K-Y, Lepadatu S, Landi S, Bending SJ, Marrows CH. Spin-Transfer-Torque-Assisted Domain-Wall Creep in a Co/Pt Multilayer Wire. *Phys Rev Lett* 2010, **104**: 137205.
34. Isasa M, Villamor E, Hueso LE, Gradhand M, Casanova F. Temperature dependence of spin diffusion length and spin Hall angle in Au and Pt. *Phys Rev B* 2015, **91**: 024402.

35. Liu L, Buhrman RA, Ralph DC. Review and Analysis of Measurements of the Spin Hall Effect in Platinum. *ArXiv* 2012, **1111.3702v3**
36. Kanazawa N, Onose Y, Arima T, Okuyama D, Ohoyama K, Wakimoto S, *et al.* Large Topological Hall Effect in a Short-Period Helimagnet MnGe. *Phys Rev Lett* 2011, **106**(15): 156603.
37. Huang SX, Chien CL. Extended Skyrmion Phase in Epitaxial FeGe(111) Thin Films. *Phys Rev Lett* 2012, **108**(26): 267201.
38. Li YF, Kanazawa N, Yu XZ, Tsukazaki A, Kawasaki M, Ichikawa M, *et al.* Robust Formation of Skyrmions and Topological Hall Effect Anomaly in Epitaxial Thin Films of MnSi. *Phys Rev Lett* 2013, **110**(11): 117202.
39. Du HF, Liang D, Jin CM, Kong LY, Stolt MJ, Ning W, *et al.* Electrical probing of field-driven cascading quantized transitions of skyrmion cluster states in MnSi nanowires. *Nat Commun* 2015, **6**: 7637
40. Kanazawa N, Kubota M, Tsukazaki A, Kozuka Y, Takahashi KS, Kawasaki M, *et al.* Discretized topological Hall effect emerging from skyrmions in constricted geometry. *Phys Rev B* 2015, **91**(4): 041122.
41. Liang D, DeGrave JP, Stolt MJ, Tokura Y, Jin S. Current-driven dynamics of skyrmions stabilized in MnSi nanowires revealed by topological Hall effect. *Nat Commun* 2015, **6**: 8217.
42. Hanneken C, Otte F, Kubetzka A, Dupe B, Romming N, von Bergmann K, *et al.* Electrical detection of magnetic skyrmions by tunnelling non-collinear magnetoresistance. *Nat Nanotechnol* 2015, **10**(12): 1039-+.
43. Heinze S, von Bergmann K, Menzel M, Brede J, Kubetzka A, Wiesendanger R, *et al.* Spontaneous atomic-scale magnetic skyrmion lattice in two dimensions. *Nat Phys* 2011, **7**(9): 713-718.
44. Hamamoto K, Nagaosa N. Electrical detection of a skyrmion in a magnetic tunneling junction. *arXiv:180304588* 2018.
45. Maccariello D, Legrand W, Reyren N, Garcia K, Bouzheouane K, Collin S, *et al.* Electrical detection of single magnetic skyrmions in metallic multilayers at room temperature. *Nat Nanotechnol* 2018, **13**(3): 233-237.

46. Raju M, Yagil A, Soumyanarayanan A, Tan AKC, Almoalem A, Auslaender OM, *et al.* Evolution of chiral magnetic textures and their topological Hall signature in Ir/Fe/Co/Pt multilayer films. *ArXiv* 2017: 1708.04084
47. Raabe J, Tzvetkov G, Flechsig U, Boge M, Jaggi A, Sarafimov B, *et al.* PolLux: A new facility for soft x-ray spectromicroscopy at the Swiss Light Source. *Rev Sci Instrum* 2008, **79**(11): 113704.

## ACKNOWLEDGEMENTS

Support from European Union (H2020 grant MAGicSky No. FET-Open-665095.103 and FP7 ITN “WALL” (Grant No. 608031), as well as from the Diamond Light Source, is gratefully acknowledged. Part of this work was carried out at the PolLux (X07DA) and SIM (X11MA) beamline of the Swiss Light Source. The PolLux end station was financed by the German Minister für Bildung und Forschung (BMBF) through contracts 05KS4WE1/6 and 05KS7WE1.

## AUTHOR CONTRIBUTIONS

CHM with KZ, SF, JR and GB conceived the experiment. SF, JR developed the STXM to incorporate transport measurements. SF, JR and GB set up the electrical measurement inside the STXM. KZ, KS, JM, SF and GB acquired the STXM and associated transport data on the discs. KZ, SF and GB analysed the STXM and electrical transport data. KZ and FAM performed the Hall bar transport measurement. KZ grew the samples and characterised the material properties. SF, AK, DB performed the PEEM and analysis. KZ performed the FEMM simulation. KZ and MCR, with support from EHL, fabricated the sample. KZ wrote the manuscript with GB and CHM. All authors reviewed the manuscript.

## AVAILABILITY OF DATA

The data associated with this paper are openly available from the University of Leeds data repository, <https://doi.org/10.5518/262>.

## COMPETING FINANCIAL INTERESTS

The authors declare no competing financial interests.

## ADDITIONAL INFORMATION

Supplementary information is available in the online version of the paper. Reprints and permission information is available online at [www.nature.com/reprints](http://www.nature.com/reprints). Correspondence and requests for materials should be addressed to KZ.

**Figure 1: Field evolution of the magnetic skyrmion.** The skyrmion measured was created using the current pulse/field protocol shown in figure S2. The skyrmion response to field is shown via the changes in **a**, Hall resistivity,  $\rho_{xy}$ , **b**, skyrmion diameter (error determined by the image resolution), and **c**, the out of plane magnetisation changes  $M_z/M_{\text{sat}}$  (the error is given by the counting statistics see supplementary information). The minor loop was repeated six times, with sixth cycle extending to high enough field, 75 mT, to finally annihilate the skyrmion. The red shaded area in **a** and **b** highlights skyrmions with a diameter of less than 75 nm which cannot be distinguished unambiguously from the saturated state using resistivity measurements. **d**, Shows a XMCD image of the skyrmion created and shown in figure S2 at 0 mT. **e-g** XMCD images of the skyrmion at 10 mT,

45 mT and 50 mT respectively, black dashed lines in **a** to **c**. The resistivity, diameter and magnetisation states correspond to the black squares and are highlighted by the black dashed lines. After the annihilation of the skyrmion shown in **d-g**, the system was returned to the saturated state and a new skyrmion was nucleated using the same current pulse and field creation protocol. **h** and **i** The XMCD image of the skyrmion at 0 mT and 24 mT, green dotted line in **a** to **c**. The resistivity, diameter and magnetisation state correspond to the green circles and the 24 mT state is highlighted by the green dotted line. Skyrmions larger than to 75 nm can be detected electrically.

**Figure 2: Multiple magnetic skyrmion creation.** Using the current and field protocol two skyrmions and three skyrmions were created. **a-c** XMCD images of two skyrmions,  $N = -2$ , at different stages of the minor field loop. **d** Shows the measured normalised resistance,  $R_{xy}/R_{xy,Sat}$ , and the extracted normalised magnetisation  $M_z/M_{Sat}$ . **e-g** Show XMCD images of two skyrmions embedded in an oppositely magnetised disc,  $N = 2$ , at different stages of the minor field loop. **h** Shows the measured normalised resistance,  $R_{xy}/R_{xy,Sat}$ , and the extracted normalised magnetisation  $M_z/M_{Sat}$ . **i-k** Show XMCD images of three skyrmions,  $N = 3$ , at different stages of the minor field loop. **l** Shows the measured normalised resistance,  $R_{xy}/R_{xy,Sat}$ , and the extracted normalised magnetisation  $M_z/M_{Sat}$ .

**Figure 3: Hall resistance signals from a single skyrmion.** **a**, Hall signal arising from the spin texture  $R_H = R_{xy} - R_N$ , normalised to the saturation value  $R_{H,Sat}$ , plotted here against the normalised magnetisation as determined from the STXM images,  $M_z/M_{Sat}$ , for the case of saturation,  $N = 0$ , one skyrmion,  $N = 1$ , two skyrmions,  $N = 2$ , two skyrmions of opposite magnetisation,  $N = -2$ , and three skyrmions,  $N = 3$ . The grey dashed line shows the expected resistance change with magnetisation if there is only an anomalous Hall resistance contribution proportional to the magnetisation. **b** Intercept resistivity,  $\rho^{Int}_{xy}$ , and slope versus the number of skyrmions extracted from linear fits to the data shown in **a**. The best linear fit to  $\rho^{Int}_{xy}$  versus  $N$  reveals a contribution of  $22 \pm 2$  n $\Omega$  cm per skyrmion. The inset shows the anomalous Hall resistivity change from saturation,  $\Delta\rho^A_{xy}$ , versus measured skyrmion radius  $r_{Sky}$  in the single skyrmion case. At radii below  $150 \pm 30$  nm,  $\rho^{Int}_{xy}$  and  $\rho^A_{xy}$ , are of comparative scale. **c** Out of plane magnetic field,  $M_z/M_{Sat}$ , and  $\rho^{Int}_{xy}$ , versus image number. The square boxes indicate magnetisation states were skyrmions states are annihilated. **d** to **o** are XMCD images at selected points, dashed lines, throughout the minor loops shown in **c**.

## METHODS

The thin films were deposited by dc magnetron sputtering in a vacuum system with a base pressure of  $2 \times 10^{-8}$  mbar and a target-substrate separation of roughly 7 cm. An argon gas pressure of 6.7 mbar was used during the sputtering and typical growth rates of around 0.1 nm/s were achieved. The superlattice stack, [Co (0.5 nm)/Ir (0.5 nm)/Pt (1.0 nm)] $_{\times 10}$ , was grown on a seed layer of Ta (3.5 nm)/Pt (3.8 nm) and capped with Pt (3.2 nm). The patterned structures were grown on 200 nm thick Si<sub>3</sub>N<sub>4</sub> membranes supported on silicon (Silson Ltd, Warwickshire, UK). An identical superlattice stack was simultaneously sputtered on thermally oxidised silicon (with oxide layer thickness of 100 nm) to provide a sample for characterisation of material properties. X-ray reflectivity was used to measure the individual layer thicknesses on this sample. Room temperature polar magneto-optical Kerr effect magnetometry and in-plane superconducting quantum interference device vibrating sample magnetometry was used to confirm the out-of-plane easy axis of the superlattice (See supplementary information figure S1 (a)). The ordinary Hall coefficient,  $R_0$ , was measured to be  $-(1.9 \pm 0.2) \times 10^{-11}$   $\Omega$ m/T using a 800 nm wide Hall bar (see supplementary information figure S1(b)).

1000 nm diameter discs were fabricated using multiple step electron beam lithography (see supplementary information figure S1(c) for scanning transmission electron microscopy image of one

of the devices measured). The lithographic recipe is described in more detail in the supplementary information.

The magnetic domains in the nanodiscs were imaged using scanning transmission x-ray microscopy (STXM) at the PoLux (X07DA) beamline at the Swiss Light Source using x-ray magnetic circular dichroism (XMCD) to provide contrast<sup>47</sup>. A spatial resolution of the order of 30 nm was achieved by using a Fresnel zone plate with an outermost zone of 25 nm to focus the x-rays on the sample. The images were taken at room temperature with the option of an out-of-plane quasi-static magnetic field. The sample surface was perpendicular to the incident x-rays, which were tuned to the Co L<sub>3</sub> absorption edge (ca. 778 eV). The x-ray magnetic dichroism contrast was measured by taking the difference between the absorption of left and right circularly polarized x-rays and dividing it by the sum of the absorption images. This leads to a black and white contrast indicating magnetic moments aligned parallel or antiparallel to the incident x-rays (see supplementary figure S1(d) for the field driven switching between the antiparallel saturation states and the corresponding Hall resistivity). The chamber was pumped down and backfilled with oxygen gas (5 mbar) to prevent carbon deposition. The disc was initially saturated at  $\pm 110$  mT. Magnetic domains were nucleated using five bipolar 500 mV/-400mV 5 ns current pulses separated by 200 ns with an approximate current density of  $7 \times 10^{11}$  A/m<sup>2</sup>. The current pulses were created using a Tektronix AWG7122C arbitrary waveform generator. The skyrmion was then created by applying a field opposing the nucleated domain magnetisation alignment until only the most stable magnetic entity was left, the skyrmion (see supplementary information figure S2). Zero field stability of this skyrmion was observed. The electrical Hall and longitudinal resistance response to expanding and shrinking the skyrmion was observed by increasing and decreasing the field in a minor loop, with a STXM image acquired corresponding to each magnetotransport data point. The field dependent diameter evolution was extracted by fitting a circle to the XMCD contrast of the skyrmions which were observed to be radially symmetric; the error was given by the spatial resolution of the measurement.

The Hall resistance of the nanodisc was measured using a four probe approach where the Hall voltage and current electrodes overlapped at the edge of the nanodisc. The longitudinal resistance used a quasi-four probe method where the electrodes were offset by 1  $\mu$ m from the disc (See supplementary figure S1 (c)). The electrodes were 500 nm in width and overlapped the edge of the disc by around 100 nm. A 17 Hz AC voltage was applied to the samples as well as a 250 mV DC voltage. The current was monitored using a 10 k $\Omega$  series resistor, R (see supplementary figure S1(c) inset). The series resistor voltage drop and Hall voltage was measured using a lock-in amplifier (Zurich Instruments model HF2LI) (see figure 1 (c) inset for a circuit diagram). The magnetoresistance was measured using a Stanford Research Systems SIM910 in conjunction with a Keithley 2000 multimeter. The Hall resistance changes in the  $N = \pm 2$  case were measured with a Keithley 2181A Nanovoltmeter. A Keithley 6221 DC and AC current source was used to apply 100  $\mu$ A and the magnetoresistance was measured using a Keithley 2400. These measurements were performed with the sample mounted inside the PoLux STXM.

A Keithley 2182 Nanovoltmeter and a Keithley 6221 DC and AC current source was used to measure the Hall voltage and magnetoresistance of the 800 nm hall bar at 285 K. The field sample was placed in a solenoid superconducting magnet to enable the application of fields up to 8 T perpendicular to the sample.

47. Raabe J, Tzvetkov G, Flechsig U, Boge M, Jaggi A, Sarafimov B, *et al.* PoLux: A new facility for soft x-ray spectromicroscopy at the Swiss Light Source. *Rev Sci Instrum* 2008, **79**(11): 113704.

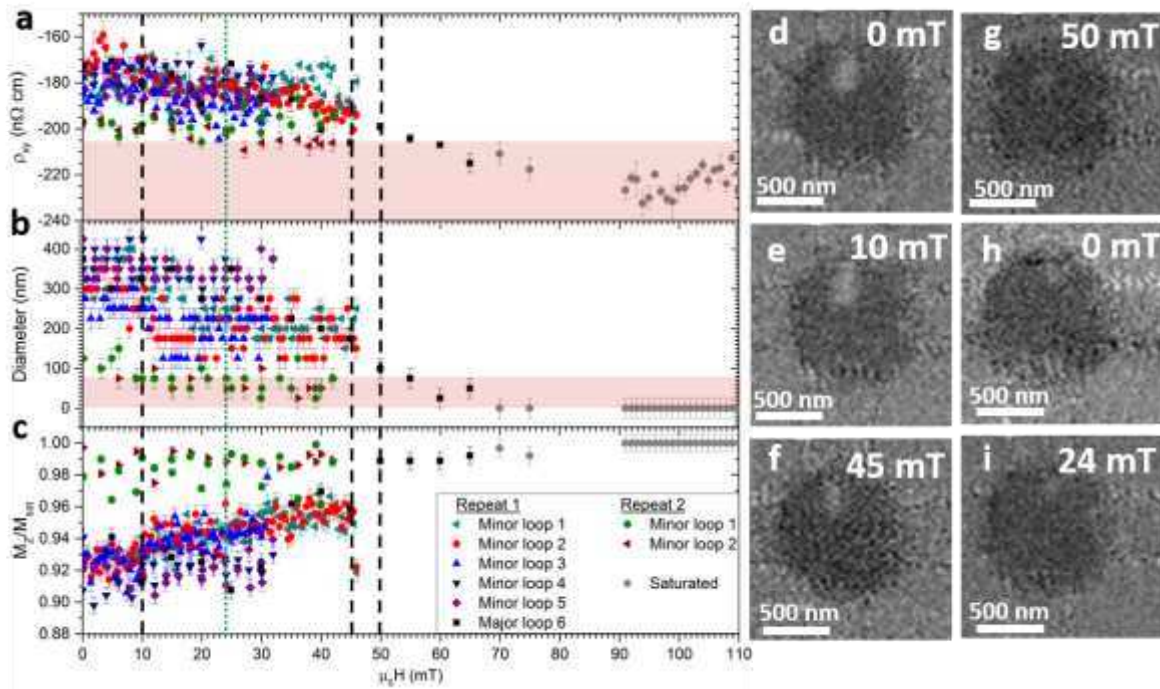


**Figure 1: Field evolution of the magnetic skyrmion.** The skyrmion measured was created using the current pulse/field protocol shown in figure S2. The skyrmion response to field is shown via the changes in **a**, Hall resistivity,  $\rho_{xy}$ , **b**, skyrmion diameter (error determined by the image resolution), and **c**, the out of plane magnetisation changes  $M_z/M_{\text{sat}}$  (the error is given by the counting statistics see supplementary information). The minor loop was repeated six times, with sixth cycle extending to high enough field, 75 mT, to finally annihilate the skyrmion. The red shaded area in **a** and **b** highlights skyrmions with a diameter of less than 75 nm which cannot be distinguished unambiguously from the saturated state using resistivity measurements. **d**, Shows a XMCD image of the skyrmion created and shown in figure S2 at 0 mT. **e-g** XMCD images of the skyrmion at 10 mT, 45 mT and 50 mT respectively, black dashed lines in **a** to **c**. The resistivity, diameter and magnetisation states correspond to the black squares and are highlighted by the black dashed lines. After the annihilation of the skyrmion shown in **d-g**, the system was returned to the saturated state and a new skyrmion was nucleated using the same current pulse and field creation protocol. **h** and **i** The XMCD image of the skyrmion at 0 mT and 24 mT, green dotted line in **a** to **c**. The resistivity, diameter and magnetisation state correspond to the green circles and the 24 mT state is highlighted by the green dotted line. Skyrmions larger than to 75 nm can be detected electrically.

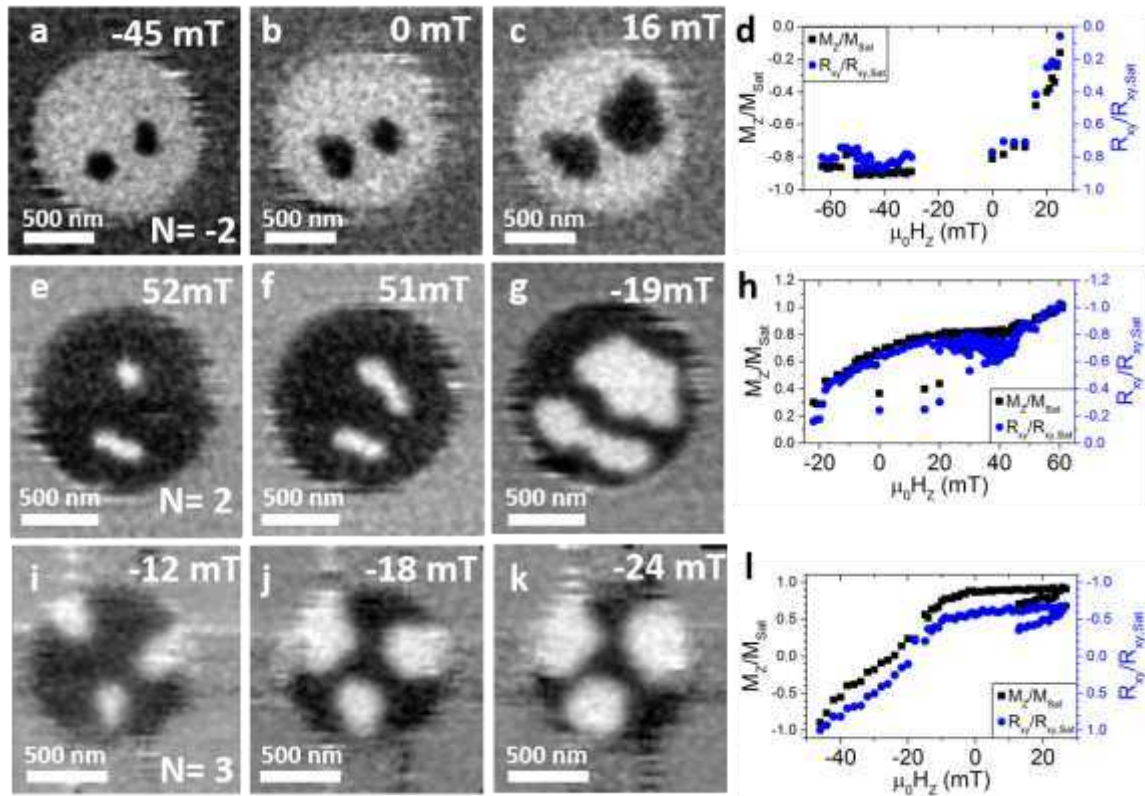


**Figure 2: Multiple magnetic skyrmion creation.** Using the current and field protocol two skyrmions and three skyrmions were created. **a-c** XMCD images of two skyrmions,  $N = -2$ , at different stages of the minor field loop. **d** Shows the measured normalised resistance,  $R_{xy}/R_{xy,Sat}$ , and the extracted normalised magnetisation  $M_z/M_{Sat}$ . **e-g** Show XMCD images of two skyrmions embedded in an oppositely magnetised disc,  $N = 2$ , at different stages of the minor field loop. **h** Shows the measured normalised resistance,  $R_{xy}/R_{xy,Sat}$ , and the extracted normalised magnetisation  $M_z/M_{Sat}$ . **i-k** Show XMCD images of three skyrmions,  $N = 3$ , at different stages of the minor field loop. **i** Shows the measured normalised resistance,  $R_{xy}/R_{xy,Sat}$ , and the extracted normalised magnetisation  $M_z/M_{Sat}$ .

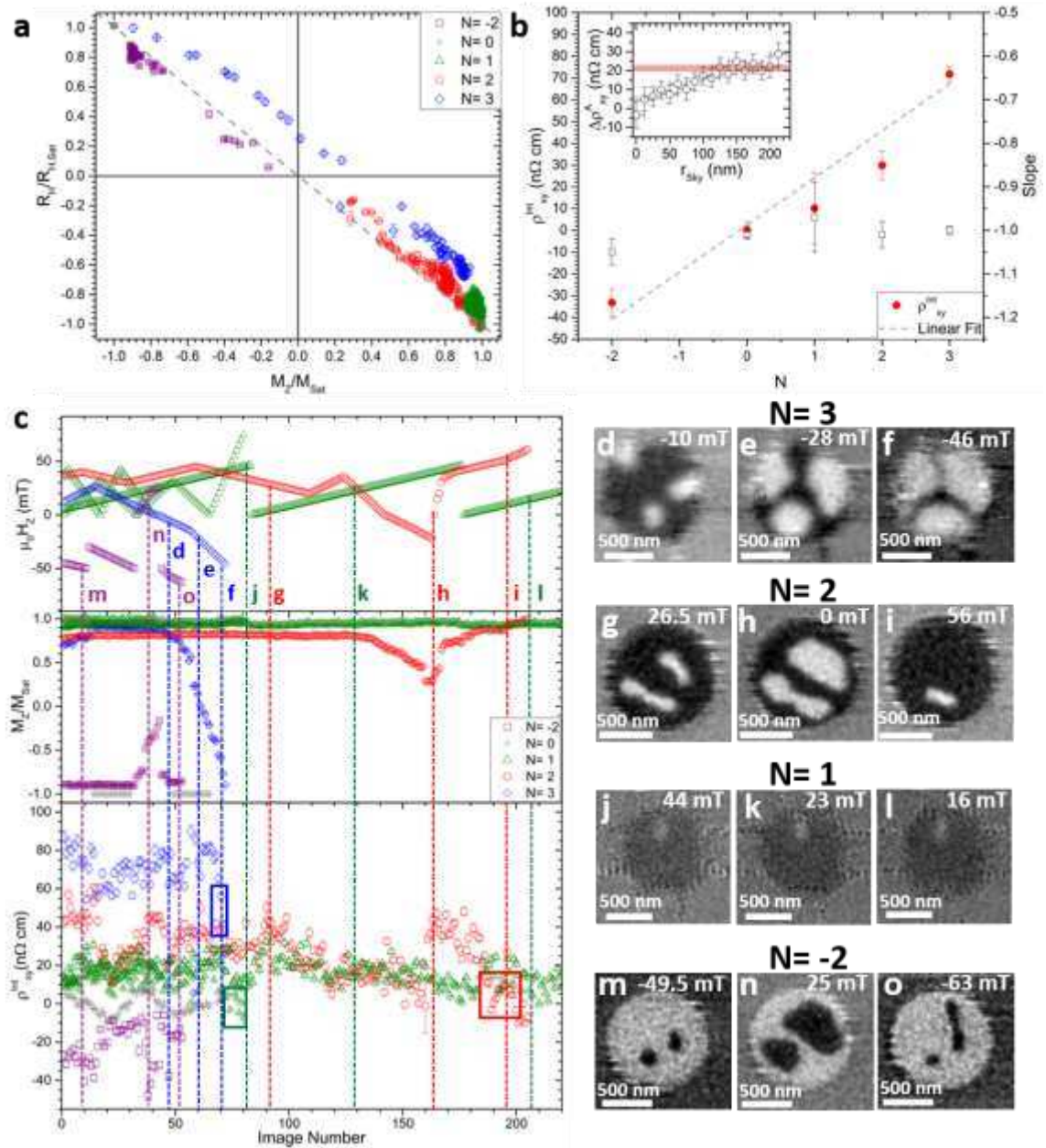


**Figure 3: Hall resistance signals from a single skyrmion.** **a**, Hall signal arising from the spin texture  $R_H = R_{xy} - R_N$ , normalised to the saturation value  $R_{H,Sat}$ , plotted here against the normalised magnetisation as determined from the STXM images,  $M_z/M_{Sat}$ , for the case of saturation,  $N = 0$ , one skyrmion,  $N = 1$ , two skyrmions,  $N = 2$ , two skyrmions of opposite magnetisation,  $N = -2$ , and three skyrmions,  $N = 3$ . The grey dashed line shows the expected resistance change with magnetisation if there is only an anomalous Hall resistance contribution proportional to the magnetisation. **b** Intercept resistivity,  $\rho_{xy}^{int}$ , and slope versus the number of skyrmions extracted from linear fits to the data shown in **a**. The best linear fit to  $\rho_{xy}^{int}$  versus  $N$  reveals a contribution of  $22 \pm 2$  nΩ cm per skyrmion. The inset shows the anomalous Hall resistivity change from saturation,  $\Delta\rho_{xy}^A$ , versus measured skyrmion radius  $r_{sky}$  in the single skyrmion case. At radii below  $150 \pm 30$  nm,  $\rho_{xy}^{int}$  and  $\rho_{xy}^A$ , are of comparative scale. **c** Out of plane magnetic field,  $M_z/M_{Sat}$ , and  $\rho_{xy}^{int}$ , versus image number. The square boxes indicate magnetisation states where skyrmions are annihilated. **d** to **o** are XMCD images at selected points, dashed lines, throughout the minor loops shown in **c**.